Enhanced thermal stability of ZrAlSiN cermet-based solar selective absorbing coatings via adding silicon element

J.-P. Meng [a, b, *], Zhou Li [a, b, *]

[a] CAS Center for Excellence in Nanoscience, Beijing Key Laboratory of Micro-nano Energy and Sensor, Beijing Institute of Nanoenergy and Nanosystems, Chinese Academy of Sciences, Beijing 100083, China
[b] School of Nanoscience and Technology, University of Chinese Academy of Sciences, Beijing 100049, China

ABSTRACT

Thermal stability is an important performance for the application of the photothermal conversion coating at high temperature. In this article, we find an effective method to improve the thermal stability of the cermet coating based on the MeAlN (Ti, Zr, Hf and so on) as absorbing layer. Adding a little Si element (~ 5 at.%) into the $Zr_{0.3}Al_{0.7}N$ (mainly absorbing layer) can modify the microstructure and form the nanocrystalline ZrAlN with amorphous-phase around it. This microstructure can suppress the spinodal decomposition of c-ZrAlN, and it benefits to decrease the nitrogen diffusion. Then, the thermal stability of coating can be improved. The novel $Cu/Zr_{0.32}Al_{0.63}Si_{0.05}N/Zr_{0.21}Al_{0.73}Si_{0.06}N/Al_{31}Si_3O_{60}N_6$ cermet coating exhibits the excellent thermal stability than the $Cu/Zr_{0.3}Al_{0.7}N/Zr_{0.2}Al_{0.8}N/Al_{34}O_{60}N_6$ cermet coating at 600°C in vacuum. It indicates that adding a little Si (~ 5 at.%) into the cermet coating based on the MeAlN (Ti, Zr and Hf and so on) as absorbing layer coating is an effective way to improve the thermal stability.

© 2019 Elsevier Ltd. All rights reserved.

Introduction

Photothermal conversion technology is an important way to harvest the solar energy directly. In photothermal conversion system, solar collector is a device which absorbs solar radiation, converts it to thermal energy, and delivers the thermal energy to a heat transfer medium [1]. As we all know, solar selective absorbing coatings can enhance the photothermal conversion efficiency of solar collector obviously. For the parabolic trough collector (PTC) applied in concentrating solar power system, solar selective absorbing coating services at high temperature (above 400°C) under vacuum. Certainly, it is important for solar selective absorbing coating to process the good chemical inertness and thermal stability at elevated temperature. In PTC system, mineral or synthetic oil is generally utilized as heat-transfer fluid (HTF). Its limitation is the low operating temperature (around 400°C) and hydrogen gas generated by the thermal decomposition [2]. Molten salt (such as

60% KNO_3+40% $NaNO_3$) is a more stabley HTF. Additionally, it can be operated at higher temperature (more than 550°C) [3–5]. The higher operating temperature is expected because the higher temperature results in the higher Cannot efficiency of power plants [6]. For PTC used molten salt as the heat-transfer fluid, a new solar selective absorbing coating which has high thermal stability and good optical properties needs to be developed.

Many coatings based on the different designed principle and physical mechanism have been developed [7]. Among those coatings, cermet coatings based on the bi-sublayer cermet film structure are demonstrated to process high absorptance and low emittance [8,9]. It becomes the preferred design system. Currently, the nitride of transition metals, such as TiN, CrN, ZrN, HfN, NbN, TiON, CrON, etc., is often chose as absorbing unite because of high thermal stability [10–16]. Generally, the nitride of transition metals (metal-like materials, absorbing unit) combined with AlN (dielectric material) is used as absorbing layer in the cermet coatings. The TiAlN is the commonly used material, whereas the c-MeAlN (Me = Ti, Zr, and Hf and so on) is a metastable phase. At high temperature, the c-MeAlN phase will transform into the c-MeN and c-AlN by the spinodal decomposition [17–21]. Then, the metastable c-AlN will transform into the stable phase h-AlN finally. During this process, the Al−N bond will break, which results in the escape and

* Corresponding authors. CAS Center for Excellence in Nanoscience, Beijing Key Laboratory of Micro-nano Energy and Sensor, Beijing Institute of Nanoenergy and Nanosystems, Chinese Academy of Sciences, Beijing 100083, China.
E-mail addresses: mengjianping@gmail.com (J.-P. Meng), zli@binn.cas.cn (Zhou Li).

loss of nitrogen atom [22]. The introduction of silicon into the MeAlN system is an effective way to modify the microstructure and properties. The formation of the amorphous Si_3N_4 on the grain boundary will refine grain and form the nanocrystalline MeAlN/ amorphous-phase nanocomposite structure which amorphous Si_3N_4 boundary layers encapsulate nanocrystalline TiAlN grains [23,24]. This structure can suppress or retard the process of spinodal decomposition and the formation of stable h-AlN at the high temperature [23,25–27]. This can suppress the escape of N, which can improve the thermal stability of cermet coatings based on the nitride of transition metals as absorbing units.

In this article, ZrN is chosen as the absorbing units. A little Si element ($\sim$ 5 at.%) is introduced into the absorbing layer to improve the thermal stability of coating. A new cermet coating of Cu/ $Zr_{0.32}Al_{0.63}Si_{0.05}N/Zr_{0.21}Al_{0.73}Si_{0.06}N/Al_{31}Si_3O_{60}N_6$ was optimization designed. Its optical properties, microstructure, and thermal stability are studied.

Experimental

The Cu, $Zr_{0.32}Al_{0.63}Si_{0.05}N$, $Zr_{0.21}Al_{0.73}Si_{0.06}N$, $Al_{31}Si_3O_{60}N_6$ films, and Cu/$Zr_{0.32}Al_{0.63}Si_{0.05}N/Zr_{0.21}Al_{0.73}Si_{0.06}N/Al_{31}Si_3O_{60}N_6$ coatings were deposited on Si(111) and glass (soda lime glass) substrates by ISB700 system. The substrates were ultrasonic cleaned with acetone and ethanol at room temperature. The single layer (Cu, $Zr_{0.32}Al_{0.63}Si_{0.05}N$, $Zr_{0.21}Al_{0.73}Si_{0.06}N$, $Al_{31}Si_3O_{60}N_6$) deposited on glass (soda lime glass) was used for the optical analysis. The films and coatings were deposited on Si(111) was for studying microstructure and thermal stability. A copper target (99.99% purity), an $Al_{90}Si_{10}$ compound target (90 at.% aluminum and 10 at.% silicon), and a zirconium target (99.9% purity) were sputtered by argon ion generated by a Kaufman ion source. The reaction ion (nitrogen ion and oxygen ion) generated by a Kaufman ion source bombarded the substrate to synthesize the $Zr_xAl_ySi_zN_{1-x-y-z}$ and $Al_{31}Si_3O_{60}N_6$ sublayers. To avoid the charge accumulation on the surface of the insulation substrate (such as Si(111) or glass), neutral filament at exit of reaction ion source was used to neutralize the nitrogen or oxygen ion. The base pressure was 2.0×10^{-4} Pa. The detail parameters were listed in Table 1. The solar selective absorbing coating has to work under a good vacuum ($\sim 10^{-2}$ Pa) at high temperature according to the concentrated ratio of solar radiation [28]. Considering the temperature fluctuation during service, the annealing temperature is 400°C and 600°C, respectively. The coating deposited on Si(111) substrate was used to carry out the annealing experiment in vacuum (5.0×10^{-2} Pa) ambient at 400°C or 600°C for different hours.

The optical constants of $Zr_{0.32}Al_{0.63}Si_{0.05}N$, $Zr_{0.21}Al_{0.73}Si_{0.06}N$, and $Al_{31}Si_3O_{60}N_6$ were measured by spectroscopic ellipsometry ((Type: M-2000UI). The detail information about the fitting process was given in supplementary. Based on the optical constants of the single layer, the reflectance spectra of the cermet coatings with

four-layer structure was optimized and calculated by a commercial optical simulation program (Version Name: TFCalc 3.5.6). The spectral reflectance in the wavelength region from 250 to 2500 nm was measured at the incidence angle of 8° by using the UV-Vis-NIR spectrophotometer equipped with an integrating sphere (Type: SHIMADZU UV3600). The reflectance in the range of 2.5−25 μm was measured by Fourier transform infrared spectrophotometer (Type: Vertex80). The total solar absorptance (α_{solar}) is obtained according to the following formula:

$$\alpha_{solar} = \frac{\int_{250}^{2500} I_{solar}(\lambda)(1 - R(\lambda))d\lambda}{\int_{250}^{2500} I_{solar}d\lambda} \tag{1}$$

where, $R(\lambda)$ is the measured reflectance from 250 nm to 2500 nm, and $I_{solar}(\lambda)$ is the ASTM AM1.5D solar spectral irradiance.

Thermal emittance ($\varepsilon_{thermal}(T)$) at the specific temperature is determined by the formula as follow:

$$\varepsilon_{thermal}(T) = \frac{\int_0^\infty I_{blackbody}(\lambda)(1 - R(\lambda))}{\int_0^\infty I_{blackbody}(\lambda)d(\lambda)} \tag{2}$$

where, $\varepsilon_{thermal}(T)$ is an emittance at the temperature T. In our article, temperature is 400°C. $I_{blackbody}(\lambda)$ is the spectral radiation of black body at 400°C according to the *Planck's radiation law*.

The microstructure of coatings is investigated by transmission electron microscope (TEM, type: Tecnai G^2 F20). The TEM is equipped with a high-angle angular-dark-field detector and X-ray energy-dispersive spectrometer systems. Element distribution in depth was measured by Auger electron spectroscopy (AES, type: ULVAC- PHI 700).

Results and discussion

The refractive index (Fig. 1a) and extinction coefficient (Fig. 1b) of the single film, including $Zr_{0.32}Al_{0.63}Si_{0.05}N$, $Zr_{0.21}Al_{0.73}Si_{0.06}N$ and $Al_{31}Si_3O_{60}N_6$, are shown in Fig. 1. The low mean-squared error (*MSE*) indicates the obtained optical constants is credible (Fig. S1, Fig. S2 and Fig. S3). In the case of $Zr_{0.32}Al_{0.63}Si_{0.05}N$ film, it is observed that there is an increase of the refractive index with the wavelength, whereas the extinction coefficient initially decreases with the wavelength, and it reaches to the minimum around 400 nm. Then, the extinction coefficient increases with wavelength and reveals a maximum at 1100 nm. These results show the metal-like behavior of $Zr_{0.32}Al_{0.63}Si_{0.05}N$ film [29]. It is the main absorbing layer. For $Zr_{0.21}Al_{0.73}Si_{0.06}N$ film, the refractive index initially reaches to the maximum at the wavelength of $\sim$ 320 nm; thereafter, it decreases. Its extinction coefficient decreases monotonically. Additionally, the extinction coefficient value is between 0.1 and 1.1.

Table 1
The deposition parameters of Cu/$Zr_{0.32}Al_{0.63}Si_{0.05}N/Zr_{0.21}Al_{0.73}Si_{0.06}N/Al_{31}Si_3O_{60}N_6$ cermet coatings.

Materials	Target	Ar (sccm)	N2 (sccm)	O2 (sccm)	AIE (keV)	ASIE (mA)	ASIE (eV)	AIC (mA)	Time (min)
$Al_{31}Si_3O_{60}N_6$	$Al_{90}Si_{10}$	5	2	4	2.7	100	200	50	14
$Zr_{0.32}Al_{0.63}Si_{0.05}N$	$Al_{90}Si_{10}$	5	6		2.7	100	200	50	3
	Zr	5			2.7	40			
$Zr_{0.21}Al_{0.73}Si_{0.06}N$	$Al_{90}Si_{10}$	5	6		2.7	100	200	50	13
	Zr	5			2.7	60			
Cu	Cu	5	0		2.7	100	200	30	10
	Cu	5			2.7	100	0	0	10

AIE, AIC, ASIE, and ASIC correspond to argon ion energy, argon ion current, assisted ion energy, and assisted ion current. $Al_{90}Si_{10}$ compound target which contains 90 at.% aluminum and 10 at.% silicon.
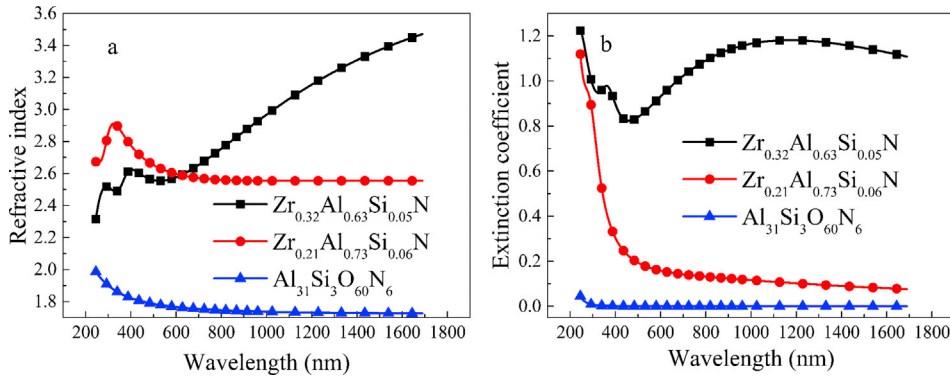
Fig. 1. Optical constants of $Zr_{0.32}Al_{0.63}Si_{0.05}N$, $Zr_{0.21}Al_{0.73}Si_{0.06}N$ and $Al_{31}Si_3O_{60}N_6$ films. (a) refractive index. (b) extinction coefficient.

Based on above results, the $Zr_{0.21}Al_{0.73}Si_{0.06}N$ exhibits an intermediate behavior (i.e. between metallic and dielectric) [30]. Both refractive index and extinction coefficient of $Al_{31}Si_3O_{60}N_6$ film decrease with wavelength. The extinction value is almost zero, which displays the dielectric behavior in nature. The low refractive index contributes to the low front surface reflections ($n_{550\ nm} = 1.7$; $R = 6.7\%$). It indicates the deposited $Al_{31}Si_3O_{60}N_6$ film is a good candidate as the antireflection layer.

A schematic diagram of the $Cu/Zr_{0.32}Al_{0.63}Si_{0.05}N/Zr_{0.21}Al_{0.73-}$ $Si_{0.06}N/Al_{31}Si_3O_{60}N_6$ cermet coating and corresponding to reflectance spectra of theoretical and experimental are shown in Fig. 2. The optical constant of Cu layer can be obtained from the standard reference [31]. After optimized design by optical simulation program, the optimized thickness of Cu, $Zr_{0.32}Al_{0.63}Si_{0.05}N$, $Zr_{0.21}Al_{0.73}Si_{0.06}N$, and $Al_{31}Si_3O_{60}N_6$ is 100 nm, 65 nm, 15 nm, and 75 nm, respectively. Then, the $Cu/Zr_{0.32}Al_{0.63}Si_{0.05}N/Zr_{0.21}Al_{0.73-}$ $Si_{0.06}N/Al_{31}Si_3O_{60}N_6$ cermet coating with approximately optimized thickness is prepared on Si(111) and glass. Comparing the theoretical and experimental reflectance spectra of coating, a good agreement between theoretical can be observed (Fig. 2). The deposited coating exhibits low reflectance (<10%) in 450 1200 nm region (the concentration area of solar radiation energy) and high reflectance in the wavelength range of 2.5–25 μm (near infrared and infrared region). The change from low to high reflectance abruptly occurred near 1100 nm. The sharp transition of reflectance indicates the deposited coatings have the excellent properties of photothermal conversion at high temperature. According to the whole reflectance from 300 nm to 28800 nm, the calculated solar absorptance is 0.945, and the thermal emittance is 0.084 at 400°C.

The cross-section and microstructure of the deposited coating was studied by TEM method. The thickness of as-deposited sublayer is approximate to the optimized thickness. Those results indicated the optical constants of sublayer is credible, and the deposited process has high controllability. The selected area electron diffraction (SAED) image of $Zr_{0.32}Al_{0.63}Si_{0.05}N$, $Zr_{0.21}Al_{0.73-}$ $Si_{0.06}N$ and $Al_{31}Si_3O_{60}N_6$ is displayed in Fig. 3b. Table 2 gives a diffraction ring analysis in terms of the corresponding phase and d-spacing. The measured d-spacing from the diffraction role of r_1 and r_2 shows that the interplanar distances of d_2 (0.2216 nm) and d_3 (0.156 nm) are assigned to the panels of c-ZrN(200) and c-ZrN(220) (PDF database file 02-0956). The measured d-spacing deviating with the theoretical values is because of the substitution of zirconium atoms by aluminum atoms which has the smaller atom radius than the atom radius of zirconium [32]. The high resolution transmission electron microscope (HRTEM) analysis of the single sublayer is carried out to investigate the sublayer microstructure. The crystalline phase of c-ZrAlN (Zone A in Fig. 3b) and amorphous phase around it can be featured in the $Zr_{0.32}Al_{0.63}Si_{0.05}N$ sublayer (Fig. 3c). In the case of $Zr_{0.21}Al_{0.73}Si_{0.06}N$ and $Al_{31}Si_3O_{60}N_6$ sublayers, the amorphous structure can be noted from Fig. 3d. Based on the above the results, the diffraction roles are from the crystalline phase in the $Zr_{0.32}Al_{0.63}Si_{0.05}N$ sublayer.

As a comparison, the microstructure analysis of the $Cu/$ $Zr_{0.3}Al_{0.7}N/Zr_{0.2}Al_{0.8}N/Al_{34}O_{60}N_6$ cermet coatings demonstrates that the $Zr_{0.3}Al_{0.7}N$ sub-layer is composed of crystalline phase of h-AlN and c-ZrAlN with a little of the amorphous phase, whereas, the $Zr_{0.2}Al_{0.8}N$ and $Al_{34}O_{60}N_6$ sub-layer are amorphous (Fig. S4) [30]. Adding 5% silicon into the $Zr_{0.3}Al_{0.7}N$ sublayer modifies the microstructure and forms the nc-ZrAlN/amorphous-phase nanocomposite [23,24]. The silicon element has little influence on the microstructure of $Zr_{0.21}Al_{0.73}Si_{0.06}N$ and $Al_{31}Si_3O_{60}N_6$ sub-layer.

The formation Gibbs energy at 298 K (ΔG^{θ}_{ZrN}) of Si_3N_4, ZrN and AlN is −665.4 kj/mol [33], −344.0 kj/mol [34], and −287.0 kj/mol [35], respectively. The nitrogen atom tends to react with the silicon
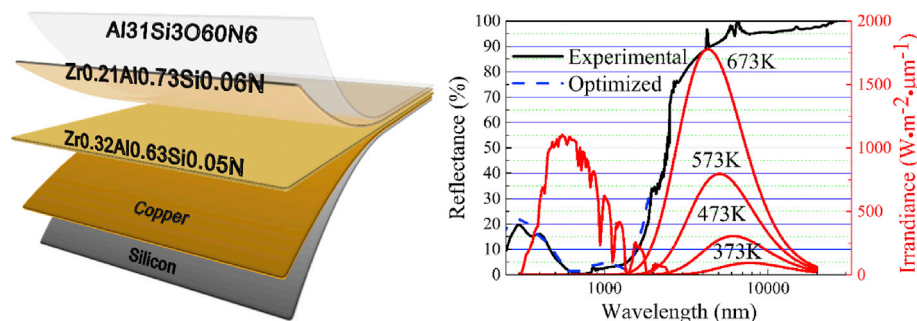

Fig. 2. Schematic diagram of the $Cu/Zr_{0.32}Al_{0.63}Si_{0.05}N/Zr_{0.21}Al_{0.73}Si_{0.06}N/Al_{31}Si_3O_{60}N_6$ absorbing coating and corresponding to optimized theoretical and experimental reflectance spectra.
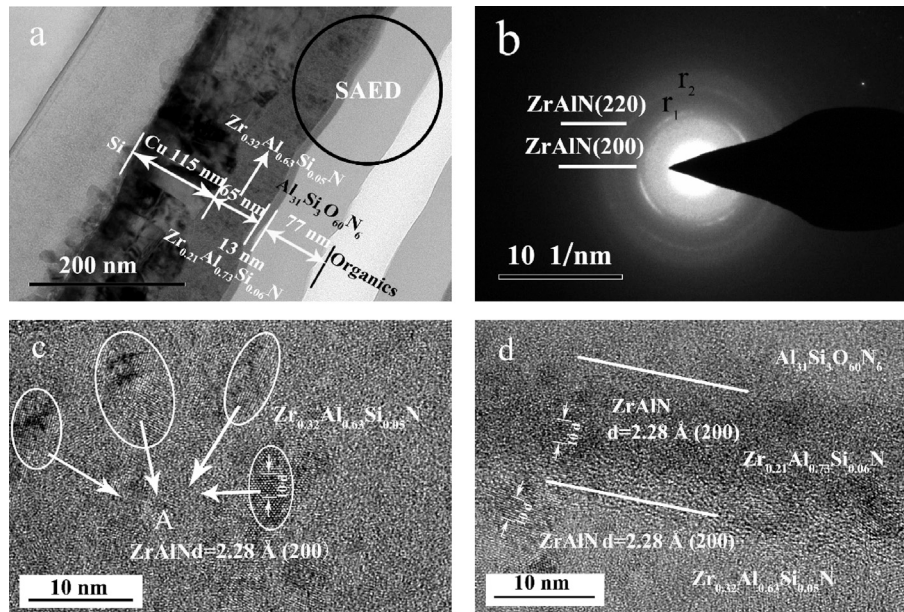
Fig. 3. The TEM analysis of as-deposited coatings: (a) TEM cross section of $Zr_{0.32}Al_{0.63}Si_{0.05}N/Zr_{0.21}Al_{0.73}Si_{0.06}N/Al_{31}Si_3O_{60}N_6$ coatings, (b) SAED image of $Zr_{0.32}Al_{0.63}Si_{0.05}N/$ $Zr_{0.21}Al_{0.73}Si_{0.06}N/Al_{31}Si_3O_{60}N_6$ layer corresponding to the area in the image of a, (c) HRTEM image of $Zr_{0.32}Al_{0.63}Si_{0.05}N$, and (d) HRTEM image of $Zr_{0.32}Al_{0.63}Si_{0.05}N/Zr_{0.21}Al_{0.73}Si_{0.06}N/$ $Al_{31}Si_3O_{60}N_6$ interface. TEM, transmission electron microscope.

Table 2
The detail information of diffraction role for as-deposited $Zr_{0.32}Al_{0.63}Si_{0.05}N/Zr_{0.21}Al_{0.73}Si_{0.06}N/Al_{31}Si_3O_{60}N_6$ coating.

Determination of diffraction rings			Phase calibration			Phase
Ring No.	nm^{-1}	Measured d-spacing (nm)	Standard d-spacing (nm)	$h\,k\,l$	Standard phase	
r_1	4.5128	0.2216	0.229	(200)	c-ZrN	c-ZrAlN
r_2	6.4102	0.1560	0.162	(220)	c-ZrN	

atom to synthesize the Si_3N_4 at substrate preferentially. The crystallinity of Si_3N_4 is poor, and Si_3N_4 tends to form amorphous. In the equilibrium thermodynamic conditions, stoichiometric fcc-ZrN and hcp(β)-Si_3N_4 are immiscible. The crystalline ZrN is synthesized. Al atom will enter into the ZrN crystal lattice by the interstitial solution, and the ZrAlN solid solution is formed. The amorphous Si_3N_4 between the nanocrystalline ZrAlN suppresses the grain growth, which will refine the grain size. The nc-ZrAlN/amorphous nanocomposites ('nc' stand for nanocrystalline) is formed. The maximum solid solubility of Al in the ZrN crystal lattice is 0.472 [36]. Additionally, the amorphous Si_3N_4 at the grain boundary of ZrAlN crystalline cuts off the template effect [37]. The abundant AlN tends to form amorphous structure. For the $Zr_{0.21}Al_{0.73}Si_{0.06}N$ sublayer, the crystal nucleus cannot grow into grain because of the low content of zirconium atom. The crystallinity of $Al_{31}Si_3O_{60}N_6$ is

poor. Hence, the sublayers of $Zr_{0.21}Al_{0.73}Si_{0.06}N$ and $Al_{31}Si_3O_{60}N_6$ are amorphous.

Thermal stability of $Cu/Zr_{0.32}Al_{0.63}Si_{0.05}N/Zr_{0.21}Al_{0.73}Si_{0.06}N/$ $Al_{31}Si_3O_{60}N_6$ coatings was performed in a vacuum ambient (5.0×10^{-2} Pa) using a tubular furnace. Table 3 gives the change of absorptance and emittance of coating after annealing treatment. The absorptance, emittance and photothermal conversion efficiency (α/ε) is almost stable. No significant change of the whole reflectance between as-deposited and coating after annealing for 192 h can be noted in Fig. 4a. Whereas, in the case of coating after annealing at 600°C, a continuous increase of emittance is observed. After annealing treatment for 192 h at 600°C, the photothermal conversion efficience efficiency (α/ε) decreases from 11.3 to 6.56. Compared with the reflectance of as-deposited coating (see Fig. 4b), the reflectance decreases above ~ 1900 nm; whereas, it keeps stable below ~ 1900 nm.

Table 3
Effect of annealing temperature and time on absorptance and emittance of $Cu/Zr_{0.32}Al_{0.63}Si_{0.05}N/Zr_{0.21}Al_{0.73}Si_{0.06}N/Al_{31}Si_3O_{60}N_6$ coating.

Condition	As-deposited	400°C 96 h	400°C 144 h	400°C 168 h	400°C 192 h
Absorptance (α)	0.945	0.946	0.945	0.943	0.943
Emittance ($\varepsilon_{400\,°C}$)	0.084	0.085	0.084	0.085	0.084
α/ε	11.3	11.1	11.3	11.1	11.2
Condition	As-deposited	600°C 96 h	600°C 144 h	600°C 168 h	600°C 192 h
Absorptance (α)	0.945	0.948	0.952	0.953	0.951
Emittance ($\varepsilon_{400°C}$)	0.084	0.093	0.107	0.123	0.144
α/ε	11.3	10.2	8.90	7.75	6.56

Fig. 4. Reflectance spectra of as-deposited and annealed $Cu/Zr_{0.32}Al_{0.63}Si_{0.05}N/Zr_{0.21}Al_{0.73}Si_{0.06}N/Al_{31}Si_3O_{60}N_6$ coatings: (a) as-deposited (black solid line) and after (red dashed line) annealing at 400°C for 192 h and (b) as-deposited (black solid line) and after (red dashed line) annealing at 600°C for 192 h.
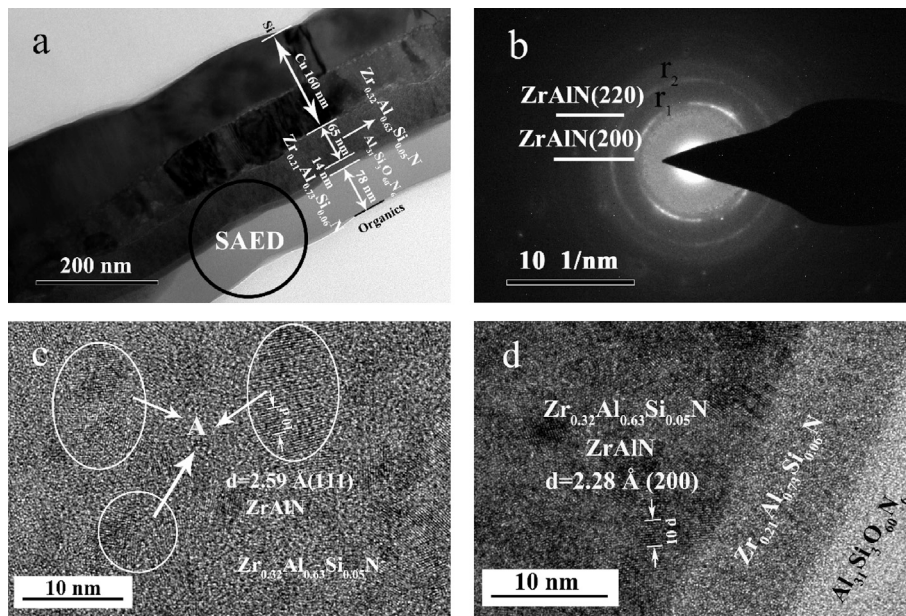

Fig. 5. The TEM analysis of annealed coating: (a) TEM cross-section of $Zr_{0.32}Al_{0.63}Si_{0.05}N/Zr_{0.21}Al_{0.73}Si_{0.06}N/Al_{31}Si_3O_{60}N_6$ coatings, (b) SAED image of $Zr_{0.32}Al_{0.63}Si_{0.05}N/Zr_{0.21}Al_{0.73}Si_{0.06}N/Al_{31}Si_3O_{60}N_6$ layer corresponding to the area in the image of a, (c) HRTEM image of $Zr_{0.32}Al_{0.63}Si_{0.05}N$, and (d) HRTEM image of $Zr_{0.32}Al_{0.63}Si_{0.05}N/Zr_{0.21}Al_{0.73}Si_{0.06}N/Al_{31}Si_3O_{60}N_6$ interface. TEM, transmission electron microscope.

The microstructure and composition analysis was carried out to study the degradation mechanism. The TEM cross-section and HRTEM images of coating after annealing at 600°C are shown in Fig. 5. After annealing treatment at 600°C, the thickness of $Zr_{0.32}Al_{0.63}Si_{0.05}N$, $Zr_{0.21}Al_{0.73}Si_{0.06}N$ and $Al_{31}Si_3O_{60}N_6$ keeps stable, and the interface is also distinguishable. The thickness increase of Cu infrared layer is because of the element diffusion between Si(111) substrate and Cu sublayer. The SAED patterns of as-deposited and annealed coating have the same feature. Table 4 gives a detail information of phase analysis. The absorbing and antireflection layer (including $Zr_{0.32}Al_{0.63}Si_{0.05}N$, $Zr_{0.21}Al_{0.73}Si_{0.06}N$ and $Al_{31}Si_3O_{60}N_6$ layer) and the structure of the crystalline phase keeps stable. No new crystal phase is observed. To confirm the microstructure further, the HRTEM analysis was implemented. The $Zr_{0.32}Al_{0.63}Si_{0.05}N$ sublayer is composed of nanocrystalline ZrAlN (Zone A in Fig. 5c) with amorphous around it. The $Zr_{0.21}Al_{0.73}Si_{0.06}N$ and $Al_{31}Si_3O_{60}N_6$ sublayers are still amorphous. The structure of absorbing and antireflection layer is stable.

The element distribution of as-deposited and annealed coating in depth was analyzed by AES. For as-deposited coating (As shown in Fig. 6a), the sublayer is distinguished clearly. The atom concentration rises and drops sharply around interface. After annealing

Table 4
The detail information of diffraction role for as-deposited $Zr_{0.32}Al_{0.63}Si_{0.05}N/Zr_{0.21}Al_{0.73}Si_{0.06}N/Al_{31}Si_3O_{60}N_6$ coating.

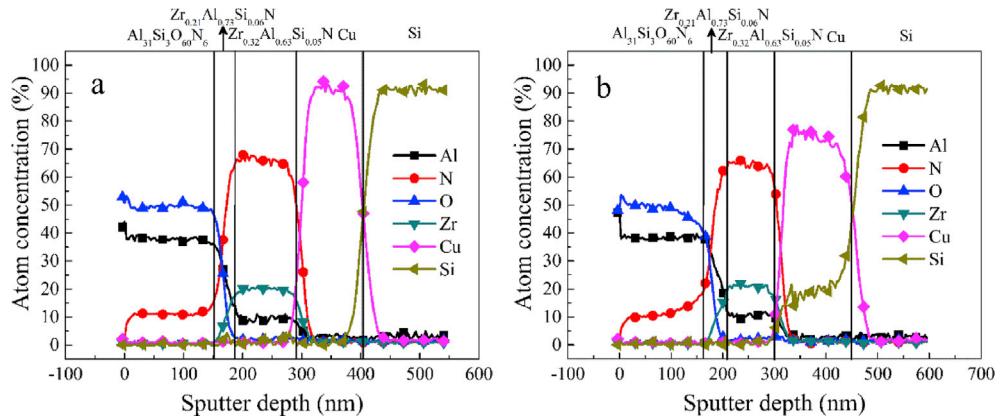| Determination of diffraction rings			Phase calibration			Phase
S	nm^{-1}	Measured d-spacing (nm)	Standard d-spacing (nm)	$h\,k\,l$	Standard phase	
r$_1$	4.5256	0.2209	0.229	(200)	c-ZrN	c-ZrAlN
r$_2$	6.3743	0.1568	0.162	(220)	c-ZrN	

Fig. 6. Depth profile of as-deposited and annealed $Cu/Zr_{0.32}Al_{0.63}Si_{0.05}N/Zr_{0.21}Al_{0.73}Si_{0.06}N/Al_{31}Si_3O_{60}N_6$ coatings (a) as-deposited and (b) annealing treatment at 600°C for 192 h.

treatment at 600°C for 192 h, the interface of absorbing layer (including $Zr_{0.32}Al_{0.63}Si_{0.05}N$ and $Zr_{0.21}Al_{0.73}Si_{0.06}N$) and antireflection layer is still distinct. The element diffuse is little. Whereas, the element diffuse between Cu infrared layer and silicon substrate is serious. For comparison, the AES result of $Cu/Zr_{0.3}Al_{0.7}N/Zr_{0.2}Al_{0.8}N/Al_{34}O_{60}N_6$ coatings after annealing treatment at 600 °C for 192 is given in the supporting information (Fig. S5). The nitrogen atoms in the $Zr_{0.3}Al_{0.7}N$ sub-layer diffuse toward into adjacent sub-layer (Cu infrared layer and $Zr_{0.2}Al_{0.8}N$ sub-layer) [30]. Comparing this results of microstructure and element distribution in depth, it can be confirmed that adding a little silicon (5 at.%) modifies the microstructure and enhanced the thermal stability.

In the Zr−Al−N system, the metastable phase of ZrAlN will transform into the stable phases c-ZrN and metastable phase c-AlN by spinodal decomposition at high temperature [17−21]. Then, the metastable phase of c-AlN will transform into the stable phase of h-AlN [18] (Fig. 7a). During this process, the escape and loss of nitrogen atom occurred because the Al−N bond will be broken [22]. The grain boundary as a channel accelerates the diffusion of nitrogen atoms [38,39]. Addition of Si into the ZrAlN can form the nc-ZrAlN/amorphous nanocomposite. This structure can suppress the process of the spinodal decomposition because of the grain refinement and amorphous between the grains [23]. Additionally,

the amorphous between the grains blocks the diffuse channel of grain boundary (Fig. 7b). Adding a little Si element into the Zr−Al−N system is an effective way to suppress the element (N or O) diffusion and improve the thermal stability. The low active diffusion energy (0.43 eV) and interstitial diffusion leads to the serious diffusion between silicon and copper at high temperature [40,41]. The formation of the Cu_3Si, Cu_5Si and $Cu_{15}Si_4$ compound owing to diffusion and reaction between silicon and copper results in the decrease of free electrons in the copper infrared layer [42,43], which decreases the infrared reflection. It leads to the emittance increase of coatings.

Conclusion

In this article, a novel $Cu/Zr_{0.32}Al_{0.63}Si_{0.05}N/Zr_{0.21}Al_{0.73}Si_{0.06}N/Al_{31}Si_3O_{60}N_6$ cermet coating which has high thermal stability has been designed and deposited. The deposited coating exhibites the high absorptance of 0.948 and the low emittance of 0.084 at 400°C. Adding a little silicon (5 at.%) into $Zr_{0.3}Al_{0.7}N$ cermet layer can change the microstructure and form the nanocrystalline ZrAlN with amorphous phase around it. This structure can suppress the spinodal decomposition of c-ZrAlN. The novel $Cu/Zr_{0.32}Al_{0.63}Si_{0.05}N/Zr_{0.21}Al_{0.73}Si_{0.06}N/Al_{31}Si_3O_{60}N_6$ exhibits the excellent thermal
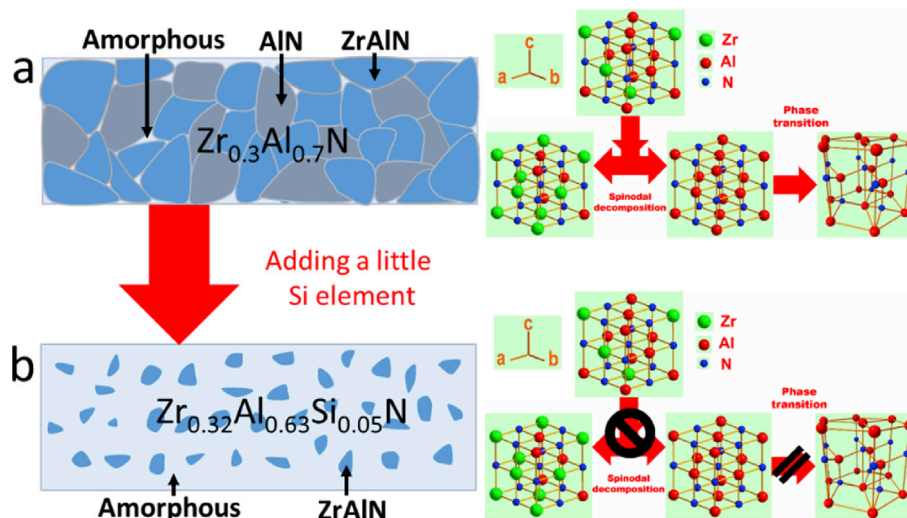

Fig. 7. Schematic diagrams of microstructural evolution and improvement of thermal stability for the $Zr_{0.32}Al_{0.63}Si_{0.05}N$ layer by adding a little silicon element. (a) the schemic of $Zr_{0.3}Al_{0.7}N$ microstructure and the phase evolutiont at 600 °C. (b) the schemic of $Zr_{0.32}Al_{0.63}Si_{0.05}N$ microstructure and the phase evolutiont at 600 °C.

stability than the $Cu/Zr_{0.3}Al_{0.7}N/Zr_{0.2}Al_{0.8}N/Al_{34}O_{60}N_6$ cermet coating at same condition. It provides an effective way to improve the thermal stability of the coating based on the MeAlN (Ti, Zr and Hf and so on) as absorbing layer.

Acknowledgments

Appendix A. Supplementary data

Supplementary data to this article can be found online at https://doi.org/10.1016/j.mtphys.2019.100131.

References

[1] F. Cao, K. McEnaney, G. Chen, Z. Ren, A review of cermet-based spectrally selective solar absorbers,, Energy Environ. Sci. 7 (2014) 1615−1627.

[2] J. Li, Z. Wang, D. Lei, J. Li, Hydrogen permeation model of parabolic trough receiver tube, Sol. Energy 86 (2012) 1187−1196.

[3] L.A. Weinstein, J. Loomis, B. Bhatia, D.M. Bierman, E.N. Wang, G. Chen, Concentrating solar power, Chem. Rev. 115 (2015) 12797−12838.

[4] F. Cao, D. Kraemer, L. Tang, Y. Li, A.P. Litvinchuk, J. Bao, G. Chen, Z. Ren, A high-performance spectrally-selective solar absorber based on a yttria-stabilized zirconia cermet with high-temperature stability,, Energy Environ. Sci. 8 (2015) 3040−3048.

[5] Z. Wu, Y. Liu, D. Wei, L. Yin, F. Bai, X. Liu, Q. Zhang, F. Cao, Enhanced spectral selectivity through the quasi-optical microcavity based on W-SiO2 cermet, Mater. Today Phys. 9 (2019) 100089.

[6] S. Chu, A. Majumdar, Opportunities and challenges for a sustainable energy future, nature 488 (2012) 294.

[7] C.G. Granqvist, Solar energy materials, Adv. Mater. 15 (2003) 1789−1803.

[8] Q.-C. Zhang, D.R. Mills, High solar performance selective surface using bi-sublayer cermet film structures, Sol. Energy Mater. Sol. Cells 27 (1992) 273−290.

[9] F. Cao, D. Kraemer, T. Sun, Y. Lan, G. Chen, Z. Ren, Enhanced thermal stability of W-Ni-Al2O3 cermet-based spectrally selective solar absorbers with tungsten infrared reflectors, Adv. Energy Mater. 5 (2015) 1401042.

[10] K. Zhang, M. Du, L. Haoa, J. Meng, J. Wang, J. Mi, X. Liu, Highly corrosion resistant and sandwich-like Si3N4/Cr-CrNx/Si3N4 coatings used for solar selective absorbing applications, ACS Appl. Mater. Interfaces 8 (2016) 34008−34018.

[11] F. Cao, L. Tang, Y. Li, A.P. Litvinchuk, J. Bao, Z. Ren, A high-temperature stable spectrally-selective solar absorber based on cermet of titanium nitride in SiO2 deposited on lanthanum aluminate, Sol. Energy Mater. Sol. Cells 160 (2017) 12−17.

[12] J.-p. Meng, X.-p. Liu, Z.-q. Fu, K. Zhang, Optical design of Cu/Zr0.2AlN0.8/ZrN/AlN/ZrN/AlN/Al34O62N4 solar selective absorbing coatings, Sol. Energy 146 (2017) 430−435.

[13] N. Selvakumar, N. Manikandanath, A. Biswas, H.C. Barshilia, Design and fabrication of highly thermally stable HfMoN/HfON/Al2O3 tandem absorber for solar thermal power generation applications, Sol. Energy Mater. Sol. Cells 102 (2012) 86−92.

[14] Y. Wu, C. Wang, Y. Sun, Y. Xue, Y. Ning, W. Wang, S. Zhao, E. Tomasella, A. Bousquet, Optical simulation and experimental optimization of Al/NbMoN/NbMoON/SiO2 solar selective absorbing coatings, Sol. Energy Mater. Sol. Cells 134 (2015) 373−380.

[15] D. Zhu, F. Mao, S. Zhao, The influence of oxygen in TiAlOxNy on the optical properties of colored solar-absorbing coatings, Sol. Energy Mater. Sol. Cells 98 (2012) 179−184.

[16] L. Wu, J. Gao, Z. Liu, L. Liang, F. Xia, H. Cao, Thermal aging characteristics of CrNxOy solar selective absorber coating for flat plate solar thermal collector applications, Sol. Energy Mater. Sol. Cells 114 (2013) 186−191.

[17] J.W. Cahn, On spinodal decomposition, Acta Metall. 9 (1961) 795−801.

[18] P.H. Mayrhofer, L. Hultman, J.M. Schneider, P. Staron, H. Clemens, Spinodal decomposition of cubic Ti1−xAlxN: Comparison between experiments and modeling, Int. J. Mater. Res. 98 (2007) 1054−1059.

[19] L. Rogström, M. Johansson, N. Ghafoor, L. Hultman, M. Odén, Influence of chemical composition and deposition conditions on microstructure evolution during annealing of arc evaporated ZrAlN thin films, J. Vac. Sci. Technol. A 30 (2012) 031504.

[20] R. Sanjinés, C. Sandu, R. Lamni, F. Lévy, Thermal decomposition of Zr1−xAlxN thin films deposited by magnetron sputtering, Surf. Coat. Technol. 200 (2006) 6308−6312.

[21] L. Rogström, L. Johnson, M. Johansson, M. Ahlgren, L. Hultman, M. Odén, Thermal stability and mechanical properties of arc evaporated ZrN/ZrAlN multilayers, Thin Solid Films 519 (2010) 694−699.

[22] M. Moser, D. Kiener, C. Scheu, P.H. Mayrhofer, Influence of yttrium on the thermal stability of Ti-Al-N thin films, Materials 3 (2010) 1573−1592.

[23] S. Veprek, H.-D. Männling, M. Jilek, P. Holubar, Avoiding the high-temperature decomposition and softening of (Al1−xTix)N coatings by the formation of stable superhard nc-(Al1−xTix)N/a-Si3N4 nanocomposite, Mater. Sci.. Eng. A 366 (2004) 202−205.

[24] P. Martin, A. Bendavid, Properties of Ti1−xSixNy films deposited by concurrent cathodic arc evaporation and magnetron sputtering, Surf. Coat. Technol. 163 (2003) 245−250.

[25] S.Q. Wang, L. Chen, B. Yang, K.K. Chang, Y. Du, J. Li, T. Gang, Effect of Si addition on microstructure and mechanical properties of Ti−Al−N coating, Int. J. Refract. Met. Hard Mater. 28 (2010) 593−596.

[26] C.-L. Chang, J.-W. Lee, M.-D. Tseng, Microstructure, corrosion and tribological behaviors of TiAlSiN coatings deposited by cathodic arc plasma deposition, Thin Solid Films 517 (2009) 5231−5236.

[27] Y.H. Yoo, D.P. Le, J.G. Kim, S.K. Kim, P. Van Vinh, Corrosion behavior of TiN, TiAlN, TiAlSiN thin films deposited on tool steel in the 3.5 wt.% NaCl solution, Thin Solid Films 516 (2008) 3544−3548.

[28] A. Antonaia, A. Castaldo, M. Addonizio, S. Esposito, Stability of W-Al2O3 cermet based solar coating for receiver tube operating at high temperature, Sol. Energy Mater. Sol. Cells 94 (2010) 1604−1611.

[29] M. Adsten, R. Joerger, K. Järrendahl, E. Wäckelgård, Optical characterization of industrially sputtered nickel−nickel oxide solar selective surface, Sol. Energy 68 (2000) 325−328.

[30] J.-p. Meng, R.-r. Guo, H. Li, L.-m. Zhao, X.-p. Liu, Z. Li, Microstructure and thermal stability of Cu/Zr0.3Al0.7N/Zr0.2Al0.8N/Al34O60N6 cermet-based solar selective absorbing coatings, Appl. Surf. Sci. 440 (2018) 932−938.

[31] J.W. Marvin, J. Weber, Handbook of Optical Materials, Laser and Optical Science and Technology Series, The CRC Press, 2003. APPENDIX V, 978−970.

[32] J.P. Meng, Z. Ke, X.P. Liu, Z.Q. Fu, L. Zhou, Influence of the aluminum content on structure and optical properties of Zr1−xAlxN films, Vacuum 145 (2017) 268−271.

[33] U. Heister, J. Krempel-Hesse, J. Szczyrbowski, G. Bräuer, New developments in the field of MF-sputtering with dual magnetron to obtain higher productivity for large area coatings, in: Proceedings of the annual technical conference-society of vacuum coaters, Society of Vacuum Coaters, 1998, pp. 187−192.

[34] W.-E. Wang, D.R. Olander, Computational thermodynamics of the Zr N system, J. Alloy. Comp. 224 (1995) 153−158.

[35] B.-Y. Shew, J.-L. Huang, The effects of nitrogen flow on reactively sputtered Ti-Al-N films, Surf. Coat. Technol. 71 (1995) 30−36.

[36] S. Sheng, R. Zhang, S. Veprek, Phase stabilities and thermal decomposition in the Zr1−xAlxN system studied by ab initio calculation and thermodynamic modeling, Acta Mater. 56 (2008) 968−976.

[37] A. Madan, I. Kim, S. Cheng, P. Yashar, V. Dravid, S. Barnett, Stabilization of cubic AlN in epitaxial AlN/TiN superlattices, Phys. Rev. Lett. 78 (1997) 1743.

[38] S. Yue, S. Yueyan, W. Fengchun, High-temperature optical properties and stability of AlxOy−AlNx−Al solar selective absorbing surface prepared by DC magnetron reactive sputtering, Sol. Energy Mater. Sol. Cells 77 (2003) 393−403.

[39] J.-P. Meng, X.-P. Liu, Z.-Q. Fu, X.-J. Wang, L. Hao, Thermal stability of AlN films prepared by ion beam assisted deposition, Appl. Surf. Sci. 347 (2015) 109−115.

[40] R. Hall, J.H. Racette, Diffusion and solubility of copper in extrinsic and intrinsic germanium, silicon, and gallium arsenide, J. Appl. Phys. 35 (1964) 379−397.

[41] J. Poate, D. Jacobson, J. Williams, R. Elliman, D. Boerma, Diffusion of implanted impurities in amorphous Si, Nucl. Instrum. Methods Phys. Res. Sect. B Beam Interact. Mater. Atoms 19 (1987) 480−483.

[42] R. Chromik, W. Neils, E. Cotts, Thermodynamic and kinetic study of solid state reactions in the Cu−Si system, J. Appl. Phys. 86 (1999) 4273−4281.

[43] S.Q. Hong, C.M. Comrie, S.W. Russell, J.W. Mayer, Phase formation in Cu-Si and Cu-Ge, J. Appl. Phys. 70 (1991) 3655−3660.